

Models of Forbidden Line Emission Profiles from Axisymmetric Stellar Winds

R. Ignace and A. Brimeyer

Department of Physics, Astronomy, & Geology, East Tennessee State University, Box 70652, Johnson City, TN 37614 USA

29 September 2018

ABSTRACT

A number of strong infrared forbidden lines have been observed in several evolved Wolf-Rayet star winds, and these are important for deriving metal abundances and testing stellar evolution models. In addition, because these optically thin lines form at large radius in the wind, their resolved profiles carry an imprint of the asymptotic structure of the wind flow. This work presents model forbidden line profile shapes formed in axisymmetric winds. It is well-known that an optically thin emission line formed in a spherical wind expanding at constant velocity yields a flat-topped emission profile shape. Simulated forbidden lines are produced for a model stellar wind with an axisymmetric density distribution that treats the latitudinal ionization self-consistently and examines the influence of the ion stage on the profile shape. The resulting line profiles are symmetric about line centre. Within a given atomic species, profile shapes can vary between centrally peaked, doubly peaked, and approximately flat-topped in appearance depending on the ion stage (relative to the dominant ion) and viewing inclination. Although application to Wolf-Rayet star winds is emphasized, the concepts are also relevant to other classes of hot stars such as luminous blue variables and Be/B[e] stars.

Key words: stars: emission line, Be – stars: mass-loss – stars: winds, outflows – stars: Wolf-Rayet

1 INTRODUCTION

Outstanding questions about the three-dimensional structure of stellar winds continue to plague our understanding of mass-loss processes from stars. Although much has been accomplished toward understanding the gross properties of stellar winds in terms of theories for spherically symmetric mass-loss (a description of current understanding along with copious references in this regard can be found in Lamers & Cassinelli 1999), a complete physical description of two and three dimensional effects remains elusive. There have been notable advances in a number of areas, with a brief and incomplete listing to include such studies as axisymmetric models of magnetized thermally driven winds (Sakurai 1985; Washimi & Shibata 1993; Sean & Balick 2004), axisymmetric line-driven winds with rotation (e.g., Bjorkman & Cassinelli 1993; Owocki, Cranmer, & Gayley 1996; Petrenz & Puls 2000), axisymmetric magnetized line-driven winds (Poe, Friend, & Cassinelli 1989; Brown et al. 2004; Ud-Doula & Owocki 2002; Townsend & Owocki 2005), axisymmetric dust-driven

winds (Asida & Tuchman 1995; Dorfi & Höfner 1996; Soker 2000), and time-dependent spherical or time-averaged spherical models (Feldmeier 1995; Dessart & Owocki 2002; Runacres & Owocki 2002, 2005). The challenge has been that to include all of the relevant physics could require multi-dimensional radiative (magneto-)hydrodynamics. Despite the difficulties involved, semi-analytic and detailed numerical models have been inspired by a large volume of observations that exhibit behavior that the steady-state spherical models are unable to explain. The examples are numerous, such as the triple rings of the SN1987A remnant (Crotts, Kunkel, & McCarthy 1989; Burrows et al. 1995; Sugerman et al. 2005), the fact that the majority of planetary nebulae and luminous blue variables are aspherical (Balick 1987; Nota et al. 1995; Davies, Oudmaijer, & Vink 2005), the existence of discs in the Be and B[e] stars (see the review of Be stars by Porter & Rivinius 2003; see the recent proceedings on B[e] stars by Kraus & Miroshnichenko 2006), discrete absorption components and related phenomena seen in hot star wind lines (Howarth & Prinja 1989; Massa et al. 1995; Brown et al. 1995; Lepine,

Moffat, & Henriksen 1996), and the inference of apparently ubiquitous clumpiness in stellar winds (Hillier 1991; Bouret, Lanz, & Hillier 2005; Fullerton, Massa, & Prinja 2006).

The goal of this contribution is to consider diagnostics of aspherical mass-loss as revealed by forbidden emission line profiles. The formation of most forbidden lines occurs over a large-scale volume of the wind. Consequently, the emission profile shapes that form in the hypersonic winds of early-type stars are imprinted with the properties of the asymptotic wind structure. This is most certainly not a new concept. Dating back to Beals (1929), it was appreciated that flat-topped emission profile shapes result for optically thin lines that form in a constant velocity and radially expanding flow. In a colliding wind binary, Stevens & Howarth (1999), Lührs (1997), Hill et al. (2000), and Hill, Moffat, & St-Louis (2002) have shown how time-dependent deviations from flat-top shaped profiles can be used as a tracer of the geometry of the colliding winds.

In this paper a parametric axisymmetric density distribution is adopted as a framework for modeling forbidden emission profiles as a function of the wind asymmetry and viewing inclination. In addition, we point out that the density function alone is not enough to completely determine emission profile shapes. The emissivity depends on the ionic species and its latitude dependence that is coupled to the overall density distribution. So our model profiles also include a treatment of the influence of latitudinal ionization effects. Interestingly, for a given stellar wind model, different lines can show different, even opposite, profile trends, as for example some lines show centrally-peaked emission, whereas others display double-peaked profiles. A number of simplifying assumptions are employed to focus on the general trends. The wind expansion is assumed constant for large radius and also in latitude. Clumping is ignored. How clumping may vary with latitude and radius in an axisymmetric hot star wind has not been well-studied, and so we choose to avoid making *ad hoc* assumptions. However, the basic equations presented here can be modified to include velocity and clumping effects to study their impact on forbidden line profile shapes.

Section 2 presents a brief overview of forbidden line formation in spherically symmetric stellar winds. Then Section 3 contains a description of the axisymmetric model, and results for model forbidden line profiles are given. Following is a summary and discussion of applications in Section 4. There are two appendices to conclude the paper. Appendix A presents an analytic solution for line profile shapes in the case of a pole-on viewing perspective of an axisymmetric wind, and Appendix B specifically shows that the two-level atom approximation that will be adopted throughout the paper applies to the particular and interesting case of NeIII for Wolf-Rayet star conditions.

2 FORMATION OF FORBIDDEN LINES IN SPHERICAL WINDS

Our presentation of the theory of forbidden line emission generally follows the approach and to some extent the notation of Osterbrock (1989) regarding the atomic physics and Barlow, Roche, & Aitken (1988) in terms of stellar wind application.

2.1 The Atomic Physics

Consider a fine structure transition for an ion species assuming a two-level atom only, denoting ‘1’ for the lower level and ‘2’ for the upper level. The level population density (number per unit volume) n_1 can be modified by collisional and radiative excitations, and the level population density n_2 can be modified by collisional de-excitations and spontaneous radiative decays. Highly non-LTE conditions exist in hot stellar winds, and so the two-level atom representation can be an excellent approximation in many cases. However, it can be the case for some atoms that there are more than two levels that can be important for the population that determines the emission for the line of interest. In the case of the Wolf-Rayet (WR) stars, the lines of [NeII] 12.8 μm ($^2P_{1/2} - ^2P_{3/2}$) and [NeIII] 15.56 μm ($^3P_1 - ^3P_2$) are of considerable interest for determining the abundance of neon. Although, the ground state of NeII is a doublet and so should be well-described by the two-level atom approximation, NeIII has five low-lying levels. The particular line at 15.56 μm happens to involve the two lowest levels of the five, and we will show later that the two-level approximation is pretty good for conditions relevant to WR stars. Thus the theory that follows assumes a two-level atom throughout.

It is commonly the case that radiative excitations from 1 to 2 are ignored compared to the collisional term. The radiative excitation rate (number per volume per second) is $n_1 B_{12} J_\nu$, with B_{12} the upward Einstein transition probability, and J_ν the mean intensity at the frequency of the line transition. The collisional rate is $n_1 n_e q_{12}$, where n_e is the electron number density and q_{12} is the collisional excitation rate in volume per second. A ratio of these rates shows that the radiative excitation rate is indeed much smaller than the collisional rate. For the wind case, J_ν will decrease with radius in the wind as the dilution factor that scales as r^{-2} , and this cancels with the electron density in the denominator that will also scale in the same way. The dominant factor that remains is a ratio $n_c/n_{e,0}$, where n_c is the ‘critical density’ and $n_{e,0}$ (to be defined in the following section) is a scale factor for the electron number density. The critical density is defined here as

$$n_c = \frac{A_{21}}{q_{21}}. \quad (1)$$

In effect, the critical density represents a transition between high density regimes with ($n_e \gg n_c$) for the line emissivity is linear in density versus low density regimes with ($n_e \ll n_c$) for which the emissivity scales with the square of density.

The volume emissivity j ($\text{erg s}^{-1} \text{cm}^{-3} \text{sr}^{-1}$) is given by

$$j = \frac{1}{4\pi} h \nu_{21} A_{21} n_2. \quad (2)$$

To determine n_2 , equilibrium conditions for the two levels are imposed as governed by the following rate expression:

$$n_1 n_e q_{12} = n_2 n_e q_{21} + n_2 A_{21}, \quad (3)$$

where

$$\frac{q_{21}}{q_{12}} = \frac{g_1}{g_2} e^\beta, \quad (4)$$

with

$$\beta = h\nu_{21}/kT_e, \quad (5)$$

for ν_{21} the frequency of the line transition, T_e the electron temperature, and g the statistical weight of the level, with $g = 2J + 1$. The collisional volume rate is given by

$$q_{21} = \frac{8.629 \times 10^{-6} \Omega_{12}}{T_e^{1/2} g_2}, \quad (6)$$

where Ω_{12} is the collision strength.

We define $n_{i,E}$ to be the number density of element E in ion stage i , and we approximate its value as

$$n_{i,E} \approx n_1 + n_2. \quad (7)$$

We make the following definitions: the ion fraction for this element in this ion stage is

$$Q_{i,E} = \frac{n_{i,E}}{\sum_1 n_{i,E}} \equiv \frac{n_{i,E}}{n_E}; \quad (8)$$

the abundance of the element relative to all nucleons is

$$\mathcal{A}_E = \frac{n_E}{n_N}, \quad (9)$$

for n_N the number density of nucleons; and the ratio of the nucleons to electrons is denoted

$$\gamma_e = \frac{n_N}{n_e}. \quad (10)$$

With these relations, the emissivity in equation (2) can be re-expressed in terms of n_e instead of n_2 . First, equation (7) is used to eliminate n_1 in equation (3), the result of which can be solved for n_2 alone, giving

$$n_2 = \frac{n_{i,E} n_e q_{12}}{n_e q_{12} + n_e q_{21} + A_{21}}. \quad (11)$$

Factoring out $n_e q_{12}$, using the definition of the critical density from equation (1) in conjunction with the preceding relations, we arrive at

$$n_2 = Q_{i,E} \mathcal{A}_E \gamma_e n_e \left\{ 1 + \frac{g_1}{g_2} e^\beta + \frac{g_1 n_c}{g_2 n_e} e^\beta \right\}^{-1} \quad (12)$$

At high densities for which $n_e \gg n_c$, one has that $j \propto A_{21} n_e$, whereas at low densities with $n_e \ll n_c$, the scaling is $j \propto A_{21} n_e^2 / n_c \propto q_{12} n_e^2$.

In Barlow et al. (1988), the quantity γ_i is defined as the *ionic fraction*, being the number density ratio of a particular ion of a particular atom to all ions in the gas. In our notation, one has that $\gamma_i = Q_{i,E} \mathcal{A}_E$. It is desirable to derive the ionic fraction to compare against stellar evolution predictions. The ionic fraction can be inferred from the observed total flux of forbidden line emission, provided that the source distance is known. If lines from different atomic species are available, line ratios can be used to derive abundances (or possibly limits to abundances) even if the source distance is not well-known.

2.2 Spherical Winds

It is instructive to briefly review the formation of forbidden lines in a spherical wind. For this purpose it is useful first to develop a sense of scale, to determine where the line emission is formed in the wind flow.

Consider a spherical wind with mass-loss rate \dot{M} and radial speed $v(r)$ for radius r . The mass density will be

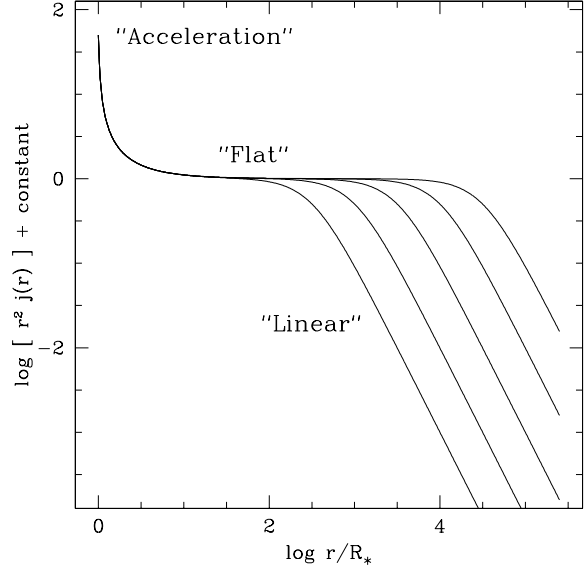


Figure 1. A logarithmic plot of the radial gradient of the line luminosity, $dL_l/dr \propto r^2 j(r)$, versus normalized radius in the wind. The curve shows three main components. The first is the ‘Acceleration’ component at far left where $v(r)$ changes from some low value at the wind base to v_∞ . Middle is the ‘Flat’ portion, where $r^2 j \propto \text{constant}$. Right is the ‘Linear’ part where $r^2 j \propto r^{-2}$. The vertical scale is shifted so that the ‘Flat’ portion is at zero. The different breaks from the flat segment to the linear portions represent line transitions with different critical densities (see text).

$$\rho_{\text{sph}} = \frac{\dot{M}}{4\pi r^2 v(r)}. \quad (13)$$

The number density will be $n_{\text{sph}} = n_N + n_e = \rho_{\text{sph}} / \bar{m}$, with $\bar{m} = \mu m_H$ the average particle mass in the wind, and μ the mean molecular weight. The electron number density is $n_e = \rho_{\text{sph}} / \mu_e m_H$, for μ_e the mean molecular weight per free electron. Similarly, the nucleon number density is $n_N = \rho_{\text{sph}} / \mu_N m_H$, for μ_N the mean molecular weight per free nucleon. In a hot star wind that is dominated by ionized hydrogen, the relations become $\bar{m} = m_H/2$, $\mu_e = \mu_N = 1$, $n_e = n_N$ and so $\gamma_e = 1$. This would be appropriate for an O star, for example. Strong forbidden lines are seen in the IR spectra of WR stars, and a WR wind is often dominated by twice ionized helium at small radii but possibly once ionized helium at large radii (e.g., Fig. 3 of Dessart et al. 2000 shows HeII is dominant for their WC8 model of WR 135). Assuming that helium is once ionized, the molecular weights become $\mu = 2$, $\mu_e = 4$, and $\mu_N = 4$, and $\gamma_e = 1$.

The region of line formation is roughly set by the radius at which the electron density and the critical density are equal. Among hot stars the mass loss rates are around $10^{-10} M_\odot \text{ yr}^{-1}$ and larger, with terminal speeds generally around 1000 km s^{-1} or greater from spectral type B and earlier (e.g., Lamers & Cassinelli 1999). We define a number density scale factor to be

$$n_0 = \frac{\dot{M}}{4\pi R_*^2 v_\infty \mu m_H}, \quad (14)$$

with values from 10^7 cm^{-3} for B star winds soaring to 10^{14} cm^{-3} in the case of dense WR winds. The critical density for a forbidden line depends on the electron number density, so we define a related scaling factor for the electron density:

$$n_{e,0} = \mu n_0 / \mu_e. \quad (15)$$

Typical stellar wind forbidden lines observed in WR winds have critical densities ranging from 10^4 to 10^7 cm^{-3} (e.g., see tab. 5 of Ignace et al. 2001). Ignoring the weaker winds with quite small \dot{M} values, the radius in the wind where $n_e = n_c$ occurs is expected to be very large. We can find this radius r_c from $n_e = (n_{e,0}) (R_*^2/r_c^2) = n_c$, giving

$$\frac{r_c}{R_*} = \sqrt{\frac{n_{e,0}}{n_c}}, \quad (16)$$

with typical values of $10^2 - 10^4$ stellar radii.

A goal of studying forbidden lines in stellar winds is to derive information about metal abundances. The observable is the total line flux that is related to the line luminosity as $F_l = L_l / 4\pi D^2$, where D is the distance to the source. Being an optically thin line, the total line luminosity depends on the atomic rates associated with the line transition and on the wind parameters, including the ionic fraction. With the atomic rates known, and the wind properties such as mass-loss rate and terminal speed provided, the observed line emission can be used to find the ionic fraction.

The total luminosity of the optically thin line emission is given by a volume integration involving the emissivity, viz

$$L_l = 4\pi D^2 F_l = 4\pi \int_{R_*}^{\infty} 4\pi r^2 j(r) dr. \quad (17)$$

Defining $\omega = (g_1/g_2) e^\beta$, then substituting equation (12) into equation (2), and this again into equation (17), one obtains

$$L_l = L_0 \int_{R_*}^{\infty} \frac{dr/R_*}{1 + \omega + \omega (r/r_c)^2}, \quad (18)$$

where

$$L_0 = 4\pi Q_{i,E} A_E \gamma_e h \nu_{21} A_{21} n_{e,0} R_*^3. \quad (19)$$

Using a change of variable with $u = R_*/r$, the integral can be re-expressed as

$$L_l = L_0 \int_0^1 \frac{du}{(1 + \omega) u^2 + \omega u_c^2}, \quad (20)$$

where $u_c = R_*/r_c$. This has an analytic solution:

$$L_l = L_0 \frac{1}{\sqrt{(1 + \omega) \omega u_c^2}} \tan^{-1} \sqrt{\frac{1 + \omega}{\omega u_c^2}}. \quad (21)$$

With ω a factor of order unity, and the expectation that $u_c^2 \ll 1$, the total luminosity generated for this forbidden line is

$$L_l \approx L_0 \frac{\pi/2}{\sqrt{(1 + \omega) \omega}} \frac{r_c}{R_*} \propto A_{21}^{1/2} n_{e,0}^{3/2}, \quad (22)$$

which is in effect the same as equation (13) of Smith & Houck (2005), except that those authors allow for a constant clumping factor (see our discussion of clumping in sect. 3.3). From

equation (22) one can easily backsubstitute to obtain the product of the ion fraction and metal abundance in terms of the measured line luminosity (for known distance):

$$Q_{i,E} A_E = \frac{(1 + \omega)^{1/2} \omega^{1/2} n_c^{1/2} L_l}{2\pi^2 \gamma_e h \nu_{21} A_{21} n_{e,0}^{3/2} R_*^3} \quad (23)$$

The reader may object that our derivation is lacking an important component of the wind, namely the inner radii where the wind accelerates. We have so far tacitly assumed a constant expansion wind at $v = v_\infty$ to derive the above result. At the inner wind, the flow accelerates from some near-hydrostatic configuration at subsonic speeds to the hypersonic speeds of order 10^3 km s^{-1} . For a typical forbidden line and a fairly dense O or WR star wind, the value of the critical radius is so large, that the contribution to the line flux from the very dense inner and accelerating wind region is negligible. To illustrate this, Fig. 1 shows the contribution function for the line luminosity. Plotted is $dL_l/dr \propto jr^2$ representing the line emission from a spherical shell as a function of the radius. A wind velocity law with the form $v(r) = v_\infty (1 - b/r)$ is assumed (with b defined so that $v = v_0$ some initial wind speed at radius $r = R_*$), such that $n_0 = 10^{13} \text{ cm}^{-3}$, and $n(R_*) \approx 10^{15} \text{ cm}^{-3}$.

At small radii, the curve is sharply dropping because of the rapidly changing velocity law. This portion is labelled the ‘Acceleration’ branch. Interior to the critical radius (where $n_e \gg n_c$), the contribution function is constant, and this branch is labelled as ‘Flat’. At large radius beyond the critical radius, the emissivity drops as the square of density, where $r^2 j \propto n_e$, and so is labelled ‘Linear’. The different breaks from the flat portion are representative of forbidden lines with different critical densities, here ranging from 10^4 cm^{-3} (break at largest radius) to 10^8 cm^{-3} (break at smallest radius).

Although the Acceleration branch shows quite a strong contribution function, it is relegated to such a narrow range of radii as compared to the location of the critical radius, that it can safely be ignored for computing the emission line flux and profile shape. What remains is a constant velocity spherical expansion flow that forms a flat-topped emission profile, which is the standard theoretical result for this case of an optically thin line (e.g., Mihalas 1978; Lamers & Cassinelli 1999). Note that the Flat and Linear portions contribute approximately equally to the total line luminosity.

3 AXISYMMETRIC WINDS

3.1 Density Structure

With a good picture of the forbidden line formation in spherical winds in mind, the case of axisymmetric flows is now addressed. To model such winds, the following parametric forms for the wind density are adopted. We assume the wind is top-bottom symmetric in what follows. Then if the equator has higher density than the pole, we use

$$n(r, \theta_*) = n_p(r) [1 + (G - 1) \sin^m \theta_*], \quad (24)$$

where the star is taken to have spherical coordinates (r, θ_*, ϕ_*) , $n_p(r)$ is the purely radius-dependent number den-

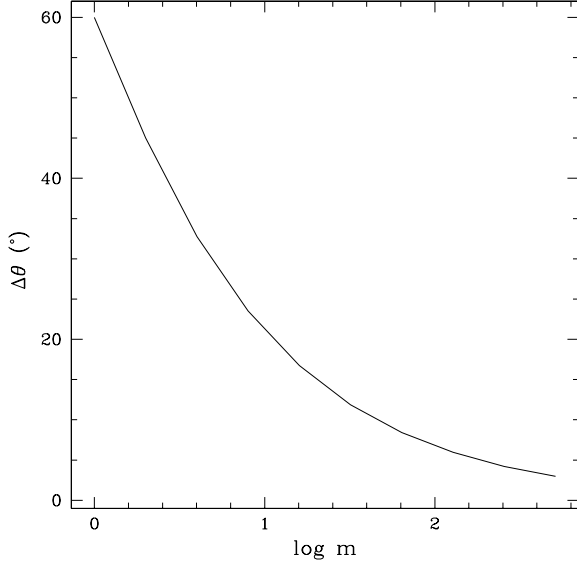


Figure 2. A plot of the effective opening angle $\Delta\theta$ of a polar or equatorial wind plotted as a function of the power exponent m .

sity distribution along the polar axis, and $G = n_{\text{eq}}/n_{\text{p}} \geq 1$ is the equator-to-pole density contrast. The latitude dependence of the density is modeled as a sine function of the co-latitude θ_* to some power m . This density function is motivated by examples of equatorial density enhancements inferred for some classes or particular stars, such as B[e] stars, or WR 134 that will be discussed later. In the case of polar enhanced wind flows, $G = n_{\text{p}}/n_{\text{eq}} \geq 1$, and we use

$$n(r, \theta_*) = n_{\text{eq}}(r) [1 + (G - 1) \cos^m \theta_*], \quad (25)$$

models that are inspired by systems like η Car and other Luminous Blue Variables that show bipolar morphologies. These density functions are not specifically related to any particular model, but are chosen as a convenient way of characterizing axisymmetric winds.

To characterize the degree of asymmetry in the wind, an opening angle $\Delta\theta$ refers to the latitude interval between either the pole or equator and the latitude at which $n(r, \theta_*) = 0.5(n_{\text{p}} + n_{\text{eq}})$. This works out in value to be the same for both polar or equatorially enhanced winds, as given by

$$\Delta\theta = \cos^{-1} (2^{-1/m}). \quad (26)$$

Values of $\Delta\theta$ are plotted in Fig. 2 against the logarithm of the power exponent m . Within this parametrization, well-confined polar or equatorial flows require quite large values of m . For example, in order to achieve $\Delta\theta \approx 5^\circ$, a value of $m \sim 10^2$ is required.

With forbidden line emission formed over a large-scale volume, we shall ignore the inner wind acceleration based on the arguments of the previous section, and treat all densities to vary as r^{-2} . To compare the spherical outflow case with the axisymmetric models, the following normalization is used:

$$n_{\text{sph}}(r) = \frac{1}{2} \int_{-1}^{+1} n(r, \theta_*) d\mu_*, \quad (27)$$

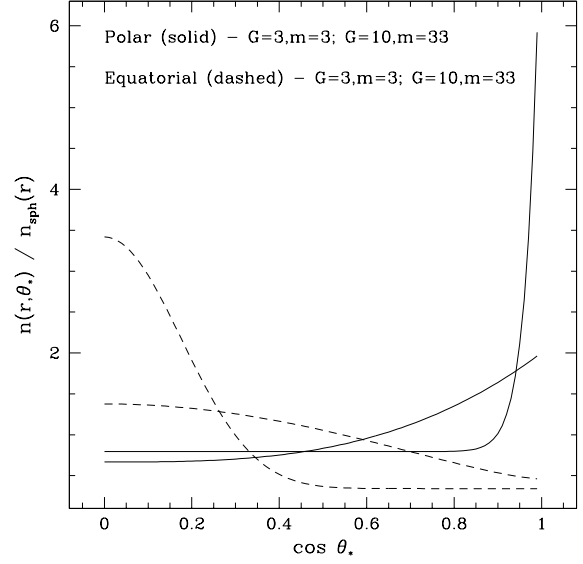


Figure 3. A plot of the latitude-dependent density normalized to the density that a spherical wind would have against stellar co-latitude. The curves are for polar enhanced (solid) and equatorially enhanced (dashed) winds for values of $G = 3$ and $m = 3$, or $G = 10$ and $m = 33$.

where $\mu_* = \cos \theta_*$. For a given value of G and m , this equation determines the ratio $H_{\text{eq}} = n_{\text{sph}}(r)/n_{\text{p}}(r)$ for a dense equatorial wind or $H_{\text{p}} = n_{\text{sph}}(r)/n_{\text{eq}}(r)$ for a dense polar wind.

To illustrate, example density profiles are plotted in Fig. 3 for different values of G and m . The density is normalized to the spherical equivalent, namely a spherical wind with the same mass-flux as the axisymmetric one. The density is plotted as a function of stellar co-latitude in $\cos \theta_*$, and so the equator is at left, and the pole at right. The solid curves are for the polar enhanced winds, and the dashed for denser equatorial winds. A brief comment on the dense polar winds versus the dense equatorial winds. When m and G are constant, n_{p} will be larger for a dense polar wind than the corresponding value of n_{eq} for a dense equatorial wind. Although the opening angle $\Delta\theta$ will be the same, the solid angle associated with the respective dense components is not equal, being smaller in the case of a polar flow.

3.2 Ionization Structure

For the ionization balance in the wind, steady-state conditions are assumed. Only radiative recombination and photoionization are considered. The ion stage i ranges from 0 to I , where ‘0’ denotes a neutral atom, and ‘ I ’ complete ionization. Since interest is focussed on forbidden lines of trace metals, the electron number density is assumed *not* to be impacted by the ionization balance of the metals. For example in O stars, hydrogen can be safely considered as completely ionized with $n_e = n_{\text{H}}$ for all radii and latitudes. For a WR wind, singly or doubly ionized helium would dominate the electron num-

6 *R. Ignace and A. Brimeyer*

ber density (although ionization of C and O is relevant for the carbon-rich WR stars). Mainly modest distortions of the wind from spherical are considered, and not dense equatorial discs or polar jets. The simplification is that with n_e given, the ionization balance for different metal species is independent.

Under these conditions, ionization equilibrium will be governed by equations of the form

$$0 = +\alpha_{i+1}(T_e) n_e n_{i+1} - \alpha_i(T_e) n_e n_i + \int_{\nu_{i-1}}^{\infty} \frac{J_\nu}{h\nu} \sigma_\nu(i-1) n_{i-1} d\nu - \int_{\nu_i}^{\infty} \frac{J_\nu}{h\nu} \sigma_\nu(i) n_i d\nu, \quad (28)$$

where the ion stages are all for the same element so that the subscript ‘E’ has been dropped, α_i is a recombination coefficient for ion i , J_ν is a mean intensity, ν_i is the photo-ionization edge frequency for ion i , and $\sigma_\nu(i)$ is the photo-ionization cross-section for ion i . In general, the equation directly couples three adjacent ion stages; implicitly all of the stages are coupled through the fact that $n_E = \sum_i n_i$. To complete the set of equations, one has that for the equation involving $i = 0$, there is no recombination to a lower ion stage, and for the case $i = I$, there is no photo-ionization to a higher ion stage.

These expressions can be simplified considerably, by assuming the diffuse radiation is negligible. The application of the theory in this paper emphasizes WR winds, and it is well-known these winds are so dense that the continuum forms in the wind itself, and a classic static photosphere is not observed. As such, the stellar radius is ill-defined, being wavelength dependent. Still we adopt a core-halo approach, in which the continuous opacity is thin beyond the radius where the continuum forms, because this is a good approximation for ascertaining the ionization balance at large radii where the forbidden line emission is generated.

To determine the ionization balance from a set of expressions based on equation (28), it is useful to define the following dimensionless parameter:

$$\delta_i = \frac{\Gamma_i}{n_{e,0}(\theta_*) \alpha_{i+1}}, \quad (29)$$

where

$$n_{e,0}(\theta_*) = \frac{\mu}{\mu_e} n_0 \left\{ \begin{array}{l} H_F^{-1} [1 + (G-1) \cos^m \theta_*] \\ H_{eq}^{-1} [1 + (G-1) \sin^m \theta_*] \end{array} \right. \quad (30)$$

for the appropriate dense polar or dense equatorial wind case. For convenience, we introduce $\delta_{-1} = 1$. The factor Γ_i pertains to the photo-ionization rate, as given by

$$\Gamma_i = \frac{1}{4} \int_{\nu_i}^{\infty} \frac{I_\nu^*}{h\nu} \sigma_\nu(i) d\nu, \quad (31)$$

where the factor of 1/4 comes from the dilution factor in the large radius limit. It is also seen that the latitude dependence for a wind with an axisymmetric density distribution enters into the ionization balance via the recombination rate terms. The ion fraction $Q_{i,E}$ will be given by

$$Q_{i,E}(\theta_*) = \frac{\prod_{j=-1}^{i-1} \delta_j}{\sum_{j=-1}^{I-1} \prod_{k=-1}^{k=j} \delta_k}. \quad (32)$$

This form also holds for the Saha equation, such as found in Mihalas (1978, eq. 5.17). However, we stress again that equation (32) for the solution of the ionization balance specifically refers to trace metals in which the electron number density is not substantially altered by the ionization balance in the element E under consideration.

It is useful to consider some special cases in relation to the structure of expression (32). Consider the condition in which there is one dominant ion stage i_0 , with $Q_{i_0} \approx 1$. The normalizations are such that as the stellar intensity is made either larger in amount or harder in energy, for a given base density n_0 , the values of δ_i will increase. As the dominant ion moves to higher stages, the lower ion stage fractions will become less significant.

Consider the expression for the dominant stage, as given by

$$Q_{i_0} = \frac{\delta_{-1} \cdots \delta_{i_0-1}}{\delta_{-1} + \delta_{-1}\delta_0 + \cdots + (\delta_{-1} \cdots \delta_{i_0-1})} \quad (33)$$

Stages with $i > i_0$ are not dominant, which can only mean that the photo-ionization rate is not large compared to the recombination rate, and so $\delta_i \ll 1$ for $i > i_0$. Since the other factors are large compared to unity (by definition, otherwise the stage i_0 could not be dominant if lower stages were not trace), then in the denominator, the normalization must be dominated by the term that involves the product $\delta_{-1} \cdots \delta_{i_0-1}$, and so clearly $Q_{i_0} \approx 1$ since the numerator and denominator have like factors.

How then will adjacent stages scale with the density? For the next lower stage and using the above argument for the dominant term in the denominator, the ion fraction will be

$$Q_{i_0-1} \approx \frac{\delta_{-1} \cdots \delta_{i_0-2}}{\delta_{-1} \cdots \delta_{i_0-1}} = \frac{1}{\delta_{i_0-1}} \propto n_0(\theta_*). \quad (34)$$

Similarly, the next higher stage will scale as

$$Q_{i_0+1} \approx \frac{\delta_{-1} \cdots \delta_{i_0}}{\delta_{-1} \cdots \delta_{i_0-1}} = \delta_{i_0} \propto [n_0(\theta_*)]^{-1}. \quad (35)$$

Thus we arrive at the general rule, in the case where there is clearly a single dominant ion stage, that

$$Q_i \propto [n_0(\theta_*)]^{i_0-i}. \quad (36)$$

This is not an especially fresh revelation. For example, the result of equation (36) with its dependence on $i_0 - i$ for the case of spherical winds can be found in spirit in the discussion of Lamers, Cerruti-Sola, & Perinotto (1987). (The scaling appears more clearly in Bjorkman et al. 1994 in their eq. [17].)

A latitude-dependent ionization balance is important for the bi-stability effect (Pauldrach & Puls 1990) for generating axisymmetric winds from the influence of stellar rotation (Lamers & Pauldrach 1991), although in this case it is a combination of a latitude-dependent stellar radiation field, mass-loss rate, and terminal speed that generates the axisymmetric wind density, whereas we are concerned with a ‘generic’ latitude-dependent density and its feedback on the ionization balance in the wind.

The radiative hydrodynamic models of Petrenz & Puls

(2000), who modeled axisymmetric line-driven winds from rotating stars, provide ion fractions with latitude (their Fig. 16). In their models the stellar radiation field is also latitude-dependent, and so impacts the ionization balance in addition to the varying wind density profile with latitude. Those authors are interested mainly in the inner wind region, where recombination and resonance lines form, and they do not consider the formation of forbidden lines at large radius.

Although we could have allowed for a stellar radiation field that was latitude-dependent, we have chosen to take the stellar radiation field as isotropic and focus on the large-scale asymptotic properties of the wind. But it should be noted that the latitude-dependence of the stellar radiation field and the latitude-dependent mass flux will not be independent, and could act to enhance or suppress the effects presented here, the question of which trend being dependent on the physics of the mass-loss processes and associated radiation transport.

3.3 Model Results

For computing a selection of model line profiles, we have chosen to focus on forbidden lines for the element of neon that are of particular interest for WR stars. The WR winds are selected because they show a number of strong forbidden emission lines in their IR spectra as revealed by ground-based and satellite observations (Barlow et al. 1988; Willis et al. 1997; Morris et al. 2000; Dessart et al. 2000; Ignace et al. 2001; Morris, Crowther, & Houck 2004), and these are important for determining metal abundances that can be used to test models of massive star evolution (e.g., Meynet & Maeder 2003). Neon is selected because lines from multiple stages of ionization of Ne can be observed in the IR, such as [NeII] and [NeIII], and possibly [NeV].

Note that our models neglect clumping, which warrants a comment or two. Although clumping is well-known to affect diagnostics of WR winds, such as recombination lines (Hillier 1991) and radio emission (Abbott et al. 1981; Nugis, Crowther, & Willis 1998), and there is a growing body of evidence that clumping also influences the less dense O star winds (Crowther et al. 2002; Bouret, Lanz, & Hillier 2005; Fullerton, Massa, & Prinja 2006), a good theoretical understanding of wind clumping is lacking, because the numerical calculations are rather complex (although there have been advances on this topic by Dessart & Owocki 2003, 2005). The details of how clumping initiates, where it initiates, how it evolves in the wind, and how it might vary in response to a latitudinal density distribution (not to mention the ionization balance) remain more or less open questions. For spherical winds a constant clumping factor is straightforward to include, such as in Dessart et al. (2000) or Smith & Houck (2005). Assuming clumping did not vary with radius or latitude, it could be included in our expressions as a simple multiplicative correction factor, but we have chosen to ignore clumping in our models for now, because of the many questions currently surrounding the details of clumping.

Table 1. Atomic Data for Neon

Recombination Rates ($10^{-12} \text{ cm}^3 \text{ s}^{-1}$)	Photo-Ionization Cross-sections ^d (10^{-18} cm^2)
—	$\sigma_0 = 58.9$
$\alpha_1^a = 0.283 \times \sqrt{10^4/T_e}$	$\sigma_1 = 14.6$
$\alpha_2^a = 1.71 \times \sqrt{10^4/T_e}$	$\sigma_2 = 2.7$
$\alpha_3^a = 4.44 \times \sqrt{10^4/T_e}$	$\sigma_3 = 3.7$
$\alpha_4^a = 9.81 \times \sqrt{10^4/T_e}$	$\sigma_4 = 0.54$
$\alpha_5^b = 25.6 \times \sqrt{10^4/T_e}$	$\sigma_5 = 0.26$
$\alpha_6^b = 42.7 \times \sqrt{10^4/T_e}$	$\sigma_6 = 0.49$
$\alpha_7^b = 65.8 \times \sqrt{10^4/T_e}$	$\sigma_7 = 0.22$
$\alpha_8^c = 320 \times \sqrt{633/T_e}$	$\sigma_8 = 0.19$
$\alpha_9^c = 616 \times \sqrt{327/T_e}$	$\sigma_9 = 0.069$
$\alpha_{10}^c = 1085 \times \sqrt{183/T_e}$	—

^a From Osterbrock (1989) ^b Based on interpolation (see text) ^c From Verner & Ferland (1996) ^d From Verner et al. (1996)

3.3.1 Ionization of Neon

We have computed the ionization balance for Ne using the semi-analytic results of equation (32). Table 1 lists the atomic data used for these computations. The recombination coefficients α_i where the subscript i refers to recombination from Ne^{+i} to the next lower ion stage, were taken from Osterbrock (1989) for $i = 1 - 4$. Values of α_i for $i = 8 - 10$ come from Verner & Ferland (1996). The remaining coefficients were computed from an interpolation of these data. The photo-ionization cross-sections are values at the respective ionization edge frequencies and were taken from Verner et al. (1996). Here the subscript refers to photo-ionization from Ne^{+i} to the next higher ion stage.

We have simplified the calculations with two assumptions: (a) the stellar radiation field is Planckian and (b) the photo-absorption cross-sections scales as $\sigma_\nu = \sigma_i (\nu_i/\nu)^3$, where σ_i and ν_i are values at the photo-absorption edge. Although these simplifying assumptions will change the detailed quantitative results of our models, they should not impact the qualitative results. For example, the scaling for the ion fractions presented in equation (36) should still hold.

An example of the ionization balance is shown in Fig. 4 for neon plotted against the wind density scaling parameter $n_{e,0}$. The radiation field is taken to be Planckian with a temperature of 40,000 K, a reasonable effective temperature for WR stars derived from detailed spectral analyses (e.g., Hamann & Koesterke 1998). It is stressed that the ion fractions are plotted against $n_{e,0}$ for different stars, and do not represent varying ion fractions as a function of wind density in a single star. For a given $n_{e,0}$, these are the ion fractions at every radius. The range of values for $n_{e,0}$ are typical for WR winds, and the dominant ion varies from Ne IV at the lower densities to Ne III at the higher densities. At this temperature, Ne II is quite trace. Smith & Houck (2001) have found that [Ne II] 12.55 microns appears in the spectra of some late WN and WC stars. For reference our models show that for a lower blackbody temperature of 30,000 K, Ne II becomes the dominant ion above $2 \times 10^{13} \text{ cm}^3$.

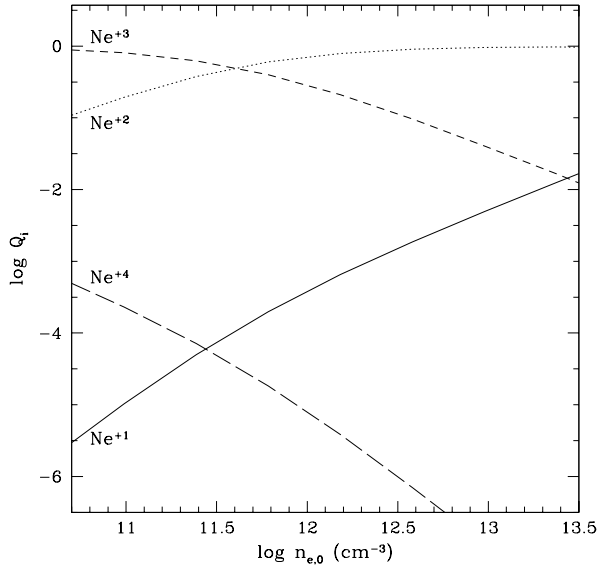


Figure 4. A plot of the ion fractions Q_i for Ne^{+i} against the base wind density scale parameter $n_{e,0}$. Ne IV is dominant for the lower densities in this plot, but Ne III becomes dominant for $n_{e,0}$ above about $3 \times 10^{11} \text{ cm}^{-3}$. As described in the text, these results assume a photoionizing spectrum from a 40,000 K blackbody.

The results of Fig. 4 are admittedly a cheat. For the dense WR winds, changing the wind density scale impacts the emergent radiation field, which has feedback for the ionization balance in the wind. So it is not really correct to fix T_{eff} at 40,000 K and allow $n_{e,0}$ to vary independently. We have computed ionization fractions based on WR spectral models provided online¹ by the Potsdam group for WN and WC stars (Gräfener, Koesterke, & Hamann 2002; Hamann & Gräfener 2003, 2004). These treat the radiation field and the wind density profile consistently. For a broad sampling of the models provided in terms of the transformed radius (Schmutz, Hamann, Wessolowski 1989) and stellar temperature, and using equation (32), the dominant ion stage is typically either NeII or NeIII, both being relatively strong forbidden lines commonly observed in the IR spectra of WR stars. Infrequently, a higher ion stage is seen to be dominant, such as NeV.

Although it would be more accurate for any given WR star to use the stellar radiation data from models like those of the Potsdam group (even better, the actual computed ionization data, but that information is not provided at their website), and to have better atomic data to relax assumption (b) above, ours is really an exploratory paper to investigate trends that axisymmetric winds will have for forbidden emission profiles. It is sufficient at this point to treat the latitude dependence of the density and ionization balance self-consistently within the stated assumptions to arrive at valid qualitative conclusions.

For an axisymmetric wind, one has $n_{e,0}$ a function of latitude. Fig. 4 indicates that changes in $n_{e,0}$ with latitude will

Table 2. Model Parameters

Figure-Panel ^a	Line Type	Ion	i	G	m
5(a), 6(a)	solid	Ne II	0°	3	5
5(a), 6(a)	dotted	Ne III	0°	3	5
5(a), 6(a)	short dash	Ne IV	0°	3	5
5(a), 6(a)	long dash	Ne V	0°	3	5
5(b), 6(b)	solid	Ne II	90°	3	5
5(b), 6(b)	dotted	Ne III	90°	3	5
5(b), 6(b)	short dash	Ne IV	90°	3	5
5(b), 6(b)	long dash	Ne V	90°	3	5
5(c), 6(c)	solid	Ne III	30°	1	3
5(c), 6(c)	dotted	Ne III	30°	2	3
5(c), 6(c)	short dash	Ne III	30°	3	3
5(c), 6(c)	long dash	Ne III	30°	9	3
5(d), 6(d)	solid	Ne III	60°	1	3
5(d), 6(d)	dotted	Ne III	60°	2	3
5(d), 6(d)	short dash	Ne III	60°	3	3
5(d), 6(d)	long dash	Ne III	60°	9	3
5(e), 6(e)	solid	Ne III	60°	3	1
5(e), 6(e)	dotted	Ne III	60°	3	3
5(e), 6(e)	short dash	Ne III	60°	3	4
5(e), 6(e)	long dash	Ne III	60°	3	8
5(f), 6(f)	solid	Ne III	0°	3	3
5(f), 6(f)	dotted	Ne III	30°	3	3
5(f), 6(f)	short dash	Ne III	60°	3	3
5(f), 6(f)	long dash	Ne III	90°	3	3

^a Fig. 5 is for the equator denser than the pole; Fig. 6 is for the pole denser than the equator. See eqns. (24) and (25).

lead to changes in the values of the ion fractions, possibly even in a shift of the dominant ion stage. So both the density and the ion fractions will change. Generally, as the base density increases, the ion fraction for a stage $i > i_0$ will tend to drop, thereby somewhat compensating for the effect of increased density on the emissivity. On the other hand if $i < i_0$, then increasing the base density will lead to a higher ion fraction, thus compounding the effect of an increased density for the emissivity.

3.3.2 Line Profile Generation

For an optically thin emission line formed over a large volume, the total line luminosity from an axisymmetric wind will be independent of the viewing inclination, and given by the following integration:

$$L_l = 8\pi^2 \int_{R_*}^{\infty} r^2 dr \int_{-1}^{+1} j(r, \theta_*) d\mu_*, \quad (37)$$

However, the emission profile shapes will depend on viewing inclination.

We had previously defined stellar spherical coordinates. We now introduce stellar Cartesian coordinates (x_*, y_*, z_*) and observer coordinates (x, y, z) . The observer is located along the positive z -axis. The viewing inclination angle i is

¹ www.astro.physik.uni-potsdam.de/PoWR.html

defined as the angle between z and the stellar symmetry axis z_* , thus $i = 0^\circ$ is a pole-on view, and $i = 90^\circ$ is edge-on. We also choose $y = y_*$ without loss of generality. The observer has spherical angular coordinates (θ, ϕ) .

The emission profile shape is given by a volume-integrated emissivity for different isovelocity zones. The isovelocity zones are defined by

$$v_z = -v_\infty \cos \theta = -v_\infty \mu, \quad (38)$$

and so are conical-shaped regions. Noting that $dv_z = -v_\infty d\mu$, combined with $d\nu = v_0 dv_z/c$ to give $d\nu = (v_\infty/\lambda_0) d\mu$, an integral expression for the profile shape $dL_1/d\nu$ becomes

$$\frac{dL_1}{d\nu}(v_z) = 4\pi \frac{\lambda_0}{v_\infty} \int_{R_*}^{\infty} r^2 dr \int_0^{2\pi} j(r, \theta_*) d\phi. \quad (39)$$

Evaluation of this integral must generally be carried out numerically (although see App. A for the special pole-on case), using the spherical trigonometric relation that for θ and ϕ given for a point in the wind, θ_* can be found from

$$\cos \theta_* = \cos \theta \cos i + \sin \theta \sin i \cos \phi. \quad (40)$$

Clearly for an arbitrary viewing inclination i , a cone of fixed θ will cut across stellar latitudes from $\theta_* = \theta - i$ to $\theta + i$, and so a particular isovelocity zone at θ will sample different densities and ion fractions.

3.3.3 Parameter Study

A number of model forbidden line profile shapes have been computed for ions of neon, and these are shown in Fig. 5 for dense equatorial winds and Fig. 6 for dense polar winds. A key to the different models displayed there is provided in Table 2. The models assume a wind dominated by HeII at large radius with $\mu = 2$, $\mu_e = 4$, a total wind density scale of $n_0 = 6 \times 10^{12} \text{ cm}^{-3}$, and an effective blackbody temperature of $T = 40,000 \text{ K}$. Figure 4 shows that Ne III will be dominant, with Ne IV down by a factor of about 10, and other ion stages inferior in abundance by much larger factors.

These parameters are roughly chosen to match the wind properties of WR 134 (Hamann & Koesterke 1998). The motivation is that WR 134 is known to have an asymmetric wind (Underhill et al. 1990; Vreux et al. 1992; Schulte-Ladbeck et al. 1992; Harries, Hillier, & Howarth 1998). The emission line of [CaIV] $3.21 \mu\text{m}$ obtained from *ISO* and discussed in Ignace et al. (2001) hints at a double-peaked emission profile, although the signal-to-noise is not very good in this weak line. Unpublished spectra of the strong HeII $3.09 \mu\text{m}$ recombination emission line in WR 134 clearly shows a well-defined, albeit asymmetric, double-peaked shape, similar to emission lines shapes that have been reported by others.

Although the basal wind density is consistent with the wind and star parameters reported by the Potsdam group, the stellar temperature of $40,000 \text{ K}$ was chosen to approximate the correct ionization balance; in fact T_* reported by Hamann & Koesterke (1998) is about twice as high, but the HeII ionization edge causes the spectrum to deviate strongly from Planckian. As discussed previously, these are simply details in light of the primary goal of highlighting qualitative profile effects.

There are six panels in Figs. 5 and 6, with each showing several line profiles. All of the emission profiles are plotted as normalized flux density against normalized Doppler shift. The flux density is related to the specific line luminosity via $dL_1/d\nu = 4\pi D^2 F_\nu$. For the normalization, the integrated flux density of the line is used so that each continuum-subtracted line-profile would have a flat-topped profile of unit height for a spherically symmetric wind. Note that each panel has a different vertical scale, indicated at the right or left side.

The panels illustrate the range of profile shapes that can result as different parameters are varied. Each panel is labeled (a)–(f) in the respective figures, and a key for the model parameters with each profile is provided in Table 2. In that table the value of G for Fig. 5 is the ratio of the equatorial to polar densities at the same radius, but for Fig. 6, G is the polar to equatorial density contrast. In both figures, the top two panels are for the extreme viewing inclinations of pole-on (left) and equator-on (right), with a mild density enhancement of $G = 3$ and a power exponent of $m = 5$. For the case of the dense polar wind seen at $i = 0^\circ$, the profiles evolve from strongly double-peaked for Ne II (solid) to modestly centrally bubbled for Ne V (long dash). Equator-on, the trend is opposite. The parameters G and m are fixed, so these are examples of reversals in the qualitative shape of the profiles as feedback from the ionization dependence on the density scale with consequence for the line emissivity. For this pole-on case, an analytic solution to the profile shapes and these scaling effects can be derived, which is provided in Appendix A.

The two middle panels are for the fixed dominant ion state of NeIII, with $m = 3$ fixed, and G allowed to vary from 1 to 9. The case $G = 1$ is spherical and so produces the flat-topped profile. The left middle panel is for a viewing inclination of $i = 30^\circ$, whereas the right middle panel is for $i = 60^\circ$. At lower left the exponent m is allowed to vary from 1 through 8 as indicated, with $G = 3$ and $i = 60^\circ$ fixed for the NeIII ion. The panel at lower right overplots profiles of $m = 3$ and $G = 3$ for NeIII as the viewing inclination varies.

There are several interesting comments and conclusions to be made from the parameter study:

(i) The profile distortions from a flat-top shape for the dense polar wind models as compared to dense equatorial winds appear more severe for a given value of G and m ; however, one must interpret this with caution. Although at fixed m , both models have the same opening angle $\Delta\theta$, this does not translate to the same solid angle. For example, if $m = 1$ for a polar wind model, then $\Delta\theta = 60^\circ$ (see eq. [26]). The relative solid angle of the dense polar wind component is $\Delta\Omega/4\pi = 0.5$. For a model with a dense equatorial wind, a structure of the same solid angle using the density parametrization of equation (24) would have $\Delta\theta = 30^\circ$ requiring $m = 4.8$. So for example to make a fair comparison of profiles between Figs. 5 and 6 as m is varied, it is the short dashed line of 5(e) that should be contrasted with the solid line of 6(e). In so doing, one finds that indeed the profile shapes are different between models of dense equatorial and dense polar winds, but the distortions from flat-top are comparable in amplitude.

(ii) Panels (a) and (b) for both Figures shows that quite strong centrally peaked or double-horned profiles do result

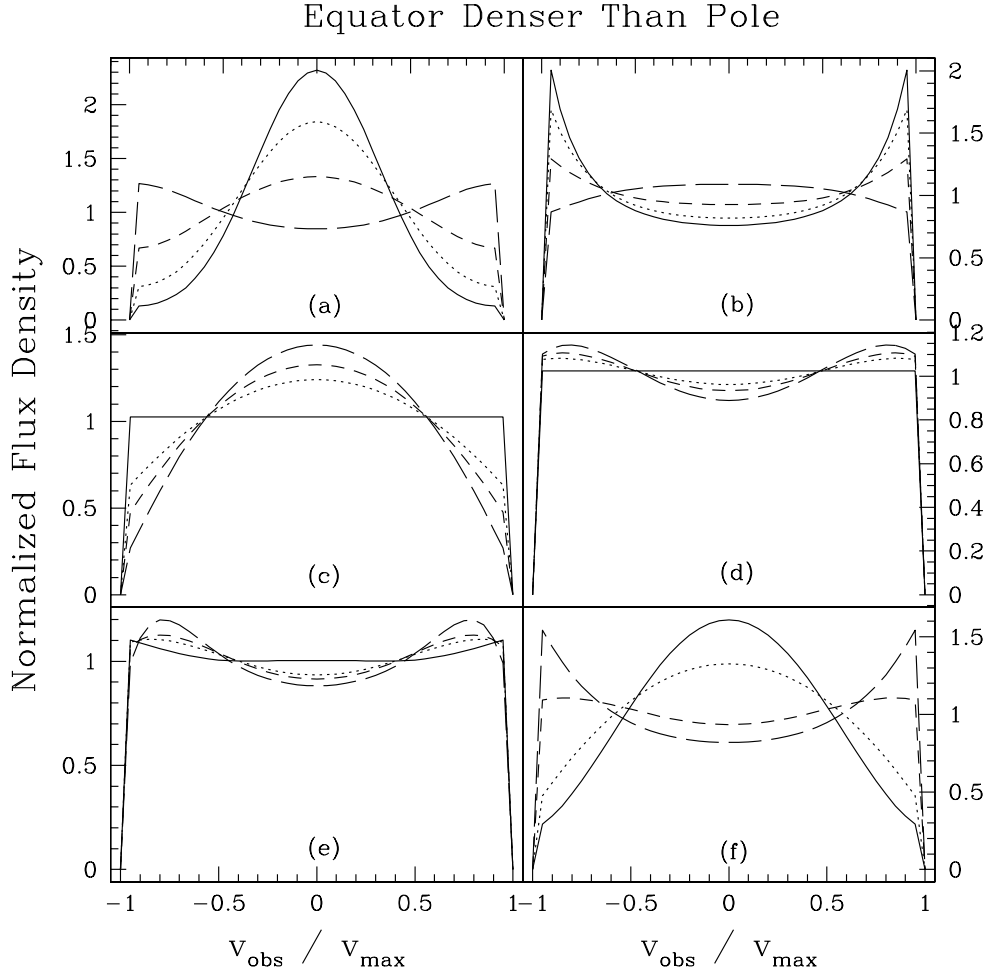


Figure 5. Model forbidden line profiles for axisymmetric winds that are more dense at the equator than the pole. Table 2 provides a listing of the model parameters and ions of neon being modeled for each of the line types in the different panels. The ordinate is normalized flux density (such that all of the emission lines have the same equivalent widths), whereas the abscissa is normalized doppler shift. Note that the vertical scale is different for each panel as indicated. The axisymmetric wind is taken to have v_{\max} the same for all latitudes, and v_{obs} varies from $-v_{\max}$ from the left side of a profile to $+v_{\max}$ at the right side of a profile. Each profile drops to zero line emission at the extreme velocity shift values.

for the dominant ion (dotted line type in these panels) for favorable viewing perspectives of pole-on or equator-on. On the other hand, mid-latitude views as shown in panels (d) and (e) for $i = 60^\circ$, statistically a probable viewing angle, reveal that distortions from flat-top shape are pretty mild, usually less than 20% deviations for the range of values in G and m shown. This is a result of the isovelocity zones, cones in this case, cutting across a fairly broad range of stellar latitudes and so sampling both high and low density regions. The end result is compensation such that the profile tends toward flat-top, unless the values of G or m become somewhat large.

(iii) The profiles have been plotted in normalized form to emphasize the impact of model parameters on line shape. However, both G and m also impact the total line flux. If the emissivity were just linear in density, then the total line emission would be conserved even though the profile shape were to deviate from flat-top. The emissivity is only linear in density for the 'flat' part; it is quadratic in the 'linear' segment of the con-

tribution function (see Fig. 1). As a result, line flux is not conserved. Indeed, it may be greater or smaller (depending on the ion stage) than an equivalent spherical wind of the same total mass-loss. For the dominant ion, line flux will be increased because of deviations from spherical flow. In general this biases ratios of line fluxes for deriving relative abundances. Specifically, if a line ratio is formed from two ions of different species but with the same value of Δi (and Δi is constant with latitude for both ions), the effect cancels, and ion fraction ratios will be the same as if the wind were spherically symmetric. So valid abundance ratios can be derived even if the wind is axisymmetric, a consequence of the line being optically thin and stellar occultation effects negligible. However, this is only true if Δi is the same for both lines, otherwise the ion fraction ratio will deviate from what would have been obtained from an equivalent spherical wind.

(iv) The model results clearly show to what extent line profiles will deviate from flat-top as model parameters are var-

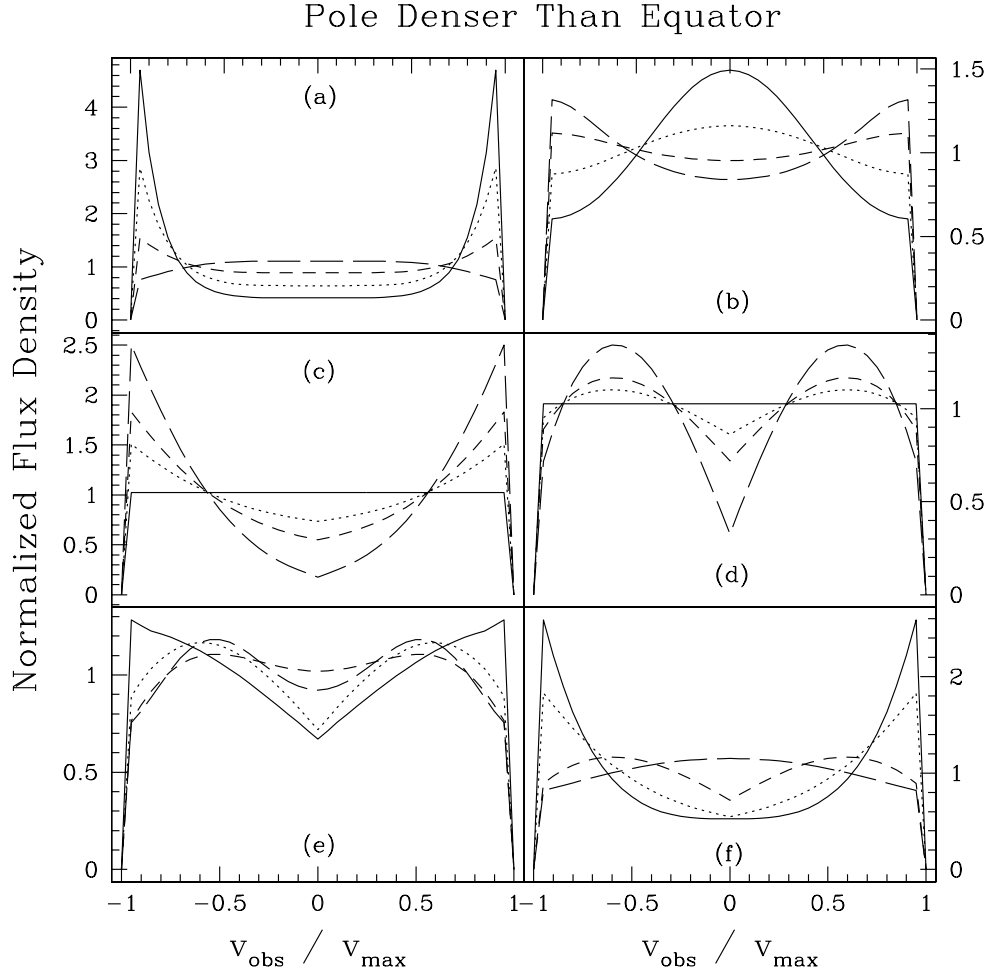


Figure 6. As in Fig. 6, but now for winds that are more dense at the poles than in the equator. Again, a key for the different line profiles is to be found in Table 2.

ied, but what can be concluded about the wind structure given an observed line profile? Without some *a priori* knowledge, there are qualitative degeneracies which combined with limited signal-to-noise data can make the inverse problem challenging. For example, changing ion stage (Δi) has effects that are similar to changing G and/or m , even toward making it ambiguous as to whether the wind is denser at the poles or the equator. Normally, based on the spectral properties, one does have an idea about the dominant ion stage.

If the ion state is roughly known, then increasing G and m tends to make the profiles display stronger deviations from a flat-top shape. Both the total line flux and the amplitude of the features (central peak or double-horns) must be matched simultaneously as G and m vary. The width of these features must also be matched, which may discriminate between dense polar versus dense equatorial models. The viewing inclination also influences the sharpness of the features as well as their location within the profile. Additional data, such as nebular morphology, polarimetry, or possibly even rotational $v \sin i$ values, may help to limit the range of viewing inclination. In practice, if the viewing inclination is intermediate of pole-on and edge-

on (as it likely will be), and the wind distortion is relatively mild, it may be hard or impossible to confidently determine the wind distortion parameters unless both the signal-to-noise and spectral resolution are quite high.

4 DISCUSSION

The objective of this study has been to consider how forbidden emission line profiles might be used as a diagnostic of the large-scale structure of stellar winds that deviate from spherically symmetric outflow. To this end, we have introduced parametric expressions for dense polar or dense equatorial axisymmetric winds. The stellar radiation field and the wind terminal speed have both been treated as isotropic, but these are assumptions that should be relaxed in producing synthetic line profiles for a particular model wind. If the mass-loss from the star varies with latitude, it is to be expected that the terminal speed will also vary, possibly correlating or anti-correlating with the mass-loss rate depending on the specifics of the wind-driving physics. In combination with the effects of the ioniza-

tion balance, deviations of the line profile shape from flat-top may be suppressed or enhanced compared to the results presented here. Relevant are the effects of clumping and velocity dispersions, such as those investigated by Runacres & Owocki (2002) for an O star model at large radius in the flow (100's of stellar radii). Exactly how such properties will vary with global asymmetries is unclear. However, for a spherical wind, if such effects persist over the scale r_c , they should be detectable in the form of sloping, in contrast to more nearly vertical, high velocity wings to the forbidden line profile shape. For aspherical winds, the expressions in this paper for thin forbidden lines can be modified to allow for a range of flow speeds and densities in a “cell-by-cell” approach to doing the numerical volume integration for the emission profile.

A particular focus of this work has been to highlight the coupling between density and ion stage which are coupled in latitude. These can act through the line emissivity to exacerbate or depress deviations of the line profile shape from a flat-top. Including the effects of a latitude-dependent radiation field and terminal speed may modify the conclusions that we have drawn from our assumed model, but the overall principle that resolved forbidden emission lines can be excellent tracers of deviations from spherical flow remains robust. At the same time, Figs. 5 and 6 do indicate that for winds with modest distortions from spherical as viewed somewhat more equator-on (the case $i = 60^\circ$) than pole-on ($i = 30^\circ$), the line profiles of the dominant stage show modest deviations from a flat-top. Combined with instrumental smearing and finite signal-to-noise, such profiles might pass as essentially flat-top.

As an observational strategy, it would be best to obtain forbidden emission line data for different ion stages within the same atom. This is not too common however, as ion stages subordinate to the dominant one can have much smaller ion fraction values and produce only weak lines. The lines of [NeII] 12.86 μm and [NeIII] 15.56 μm are an example of a pair of forbidden lines in adjacent ion stages that can both be seen in WR star winds (see App. B for a discussion of the applicability of the two-level atom approximation for NeIII). *ISO* observed WR stars with high spectral resolution at the appropriate wavelengths, but only a few such stars were observed. One example showing both forbidden lines is WR 11 (van der Hucht et al. 1996), but this is a colliding wind binary system. Both lines were also seen in the luminous blue variable, P Cygni (Lamers et al. 1996). Already *Spitzer* has observed a number of WR stars with the IRS; unfortunately, the IRS generally has inadequate spectral resolution to analyze the line profile shapes to apply the results of this paper. An exception to this might be the extremely fast, but also extremely rare, winds of the oxygen-rich WO subtype ((Barlow & Hummer 1982; Kingsburgh et al. 1995). These winds sport terminal speeds upwards of 3000 km/s (e.g., Drew et al. 2004). Forbidden lines observed at high resolution with the IRS for the WO stars may be suitable to determine or place limits (subject to the signal-to-noise) on the geometry of the asymptotic structure of these winds. These are hotter stars, so instead of [Ne III], perhaps IR lines of [Ne V] will be present.

ACKNOWLEDGEMENTS

This research was conducted in part through a summer REU program, for which Adam Brimeyer expresses grateful appreciation to the SARA REU program and the National Science Foundation. This research was supported in part by a grant award to the Florida Institute of Technology by the NSF (AST-0097616). The authors also thank Drs Gary Henson, and Joe Cassinelli, and Martin Hendry for helpful comments pertaining to this study. Ignace is particularly grateful to Ken Gayley for discussions in the early part of this study. The authors are also very appreciative of an anonymous referee who made several helpful comments that significantly clarified the presentation of results.

APPENDIX A: ANALYTIC LINE PROFILES FOR A POLE-ON INCLINATION

The latitude dependence of the axisymmetric density distribution is described by

$$f(\theta_*) \equiv n(r, \theta_*)/n_{\text{sph}}(r) = H^{-1} [1 + (G - 1)g(\theta_*)], \quad (\text{A1})$$

where H is a normalization set by eq. (27), and $g(\theta_*) = \cos^m \theta_*$ for a dense polar wind or $\sin^m \theta_*$ for a dense equatorial wind.

In the case of a pole-on viewing inclination with $i = 0^\circ$, one has that $\theta = \theta_*$. The emission line profile shape is then determined by

$$\frac{dL_l}{d\nu} \propto \int_{R_*}^{\infty} n_2(r) r^2 dr \quad (\text{A2})$$

$$\propto \int_{R_*}^{\infty} \frac{n_e Q_i}{1 + n_c/n_e} r^2 dr \quad (\text{A3})$$

Using eq. (36) and defining $\Delta i = i - i_0$, we have that

$$\frac{dL_l}{d\nu} \propto \int_{R_*}^{\infty} \frac{f^{1-\Delta i}}{1 + f r^2/r_c^2} dr \quad (\text{A4})$$

$$= \int_0^1 f^{1-\Delta i} (u^2 + f^{-1} u_c^2)^{-1} du \quad (\text{A5})$$

where the last line involves a substitution of $u = R_*/r$ and the lower limit to the integral assumes $u_c = R_*/r_c \ll 1$. This last integral has an analytic solution:

$$\frac{L_l}{d\nu} \propto [f(\theta_*)]^{1.5-\Delta i}. \quad (\text{A6})$$

Since $\theta = \theta_*$, and the observed doppler shifted velocity in the profile is $v_z = v_{\text{max}} \cos \theta$, one has that $\cos \theta_* = v_z/v_{\text{max}}$, that can be substituted in for $g(\theta_*)$ to derive an analytic function for the emission profile shape.

Example profiles based on equation (A6) are shown in Fig. A1. The upper panel is for a dense polar wind, and the lower one for a dense equatorial wind. Similar to Figs. 5 and 6, the line types are for $\Delta i = -1$ (solid), 0 (dotted), +1 (short dash), +2 (long dash). In those Figures, [Ne III] was the dominant ion stage for neon, but here Fig. A1 is for any metal species. Unlike Figs. 5 and 6, a profile for $\Delta i = -2$ has been

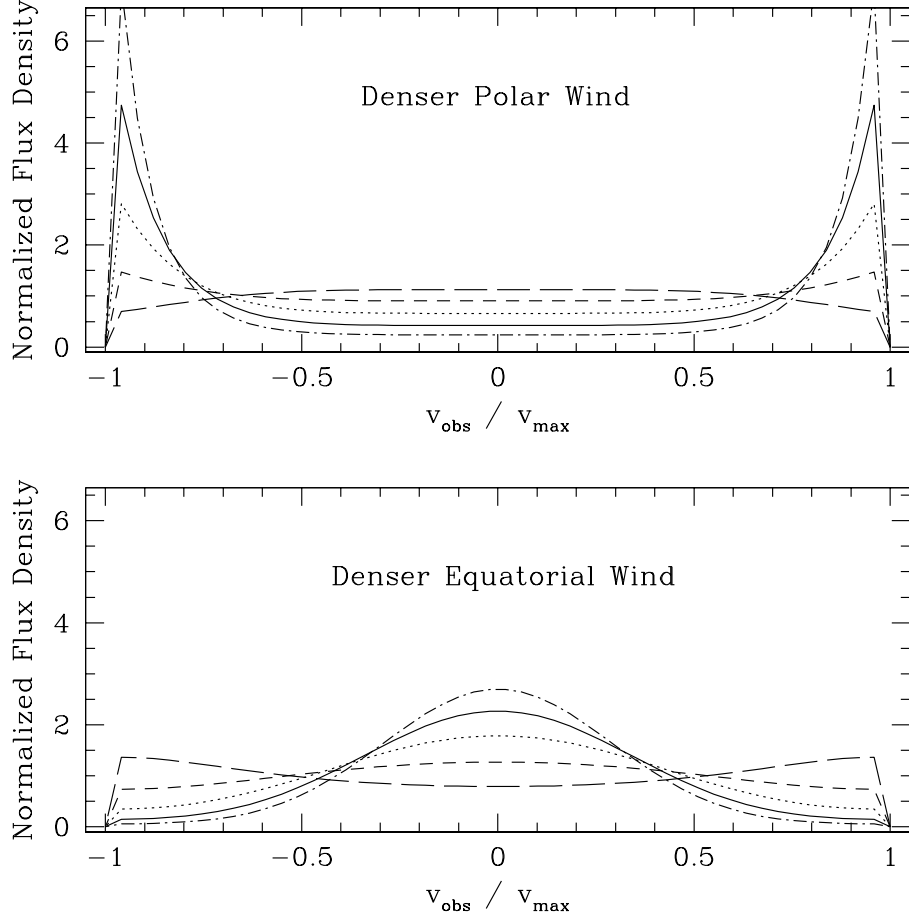


Figure A1. Analytic solutions for forbidden line profile shapes as seen pole-on. Upper is for a dense polar wind, and lower is for a dense equatorial wind. For the dense polar wind of the upper panel, profiles progressively shift from a strongly double-horned emission shape with $\Delta i = -2$ to one that is mildly centrally peaked at $\Delta i = +2$. The exact opposite progression occurs for a dense equatorial wind in the lower panel. Values of $m = 5$ and $G = 3$ were adopted, and the profiles are normalized so that a spherical wind would produce a profile of unit height in this figure.

computed for Fig. A1, and is shown as dot-dash line type. In all these cases, values of $G = 3$ and $m = 5$ were used. The profiles are normalized by their total emission.

In the case of the dense polar wind as viewed pole-on, the profiles for the dominant ion stage and lower stages are substantially double-peaked, because f is large along the poles. Even though G has a modest value, these profiles depend on f in powers of 1.5, 2.5, and 3.5, so that strong double-horned profiles still result. In contrast, the profiles at $\Delta i = +1$ and $+2$ show a slight double-horned structure in the first case and a centrally bubbled one in the second. Both of these appear nearly flat-topped owing to the weak dependence on f at $f^{-0.5}$ and $f^{+0.5}$, respectively.

In contrast, the profiles for the dense equatorial flows (lower panel) are all centrally peaked, except for one that shows a modest double-horned morphology. Here the denser flow is mostly in the plane of the sky corresponding to observed velocity shifts around line center. For the dominant ion stage and lower, this leads to modest or strong central peaks

relative to a flat-topped profile and substantially depressed emission wings. Interestingly, the depressed wings could make the determination of the true line width problematic owing to uncertainties in the continuum placement for modest signal-to-noise data. Once again, as seen in the upper panel, the profiles for 1 and 2 stages above the dominant ion approach a somewhat more flat-top appearance, and switches from centrally peaked emission for $\Delta i = +1$ to the double-horned appearance for $\Delta i = +2$.

APPENDIX B: NEIII AND THE TWO-LEVEL ATOM APPROXIMATION

The derivations of this paper are predicated on the assumption of a two-level atom. A forbidden line of considerable interest from WR stars is the [NeIII] 15.55 μm line ($^3\text{P}_1 - ^3\text{P}_0$), which is seen to be strong in a number of WR stars from observations by *ISO* (Morris et al. 2000; Dessart et al. 2000) and

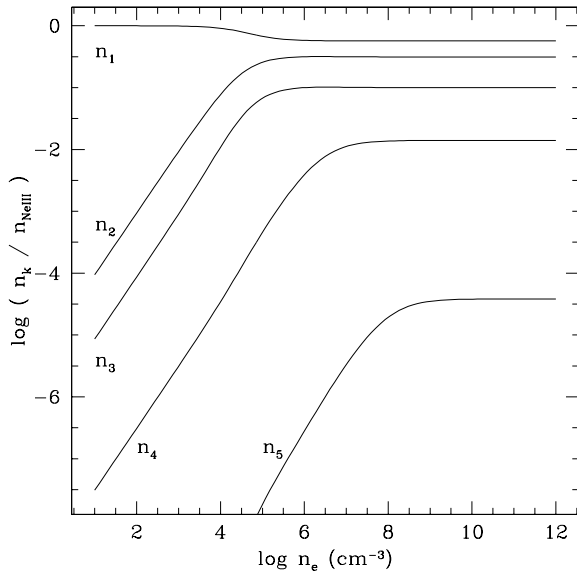


Figure B1. A plot of normalized level population number densities for the five lowest energy levels in NeIII. Assuming highly NLTE conditions, the population in all levels greater than these five are taken to be negligible. The transition 2 – 1 corresponds to the forbidden line of [NeIII] 15.55 μm , and this figure shows in large part, this atom can be reasonably approximated as a two-level atom for conditions relevant to WR star winds.

Spitzer (Morris et al. 2004; Cassinelli, private comm.). However, NeIII has five low-lying energy levels, that are (in order of increasing energy): $^3\text{P}_0$, $^3\text{P}_1$, $^3\text{P}_2$, $^1\text{D}_2$, and $^1\text{S}_0$. The question is then, how bad is the two-level approximation for NeIII?

Population number densities for these five levels, denoted 1-5 in the order listed above, have been computed, and the results are displayed in Fig. B1. To derive the populations, the equations of statistical equilibrium were solved allowing for collisional excitation and de-excitation, and radiative decay. Being interested primarily in the large radius conditions, the electron temperature was taken to be $T_e = 10,000$ K. Atomic data were taken from Pradhan & Peng (1994). Absorption and stimulated emission were included, assuming a blackbody radiation spectrum, but as expected, these were found to have no impact on the level populations.

Fig. B1 shows that $n_1 + n_2 \approx n(\text{Ne III})$ is reasonably accurate, with an error not exceeding 10% at densities higher than the critical density, and for densities near and below the critical value, the error becomes negligibly small as $n_1 \rightarrow n(\text{Ne III})$. This conclusion suggests that if Ne III is the dominant ion, then neon abundances can safely be derived from the 15.55 μm line in the two-level atom approximation, with a correction that is probably comparable or less than measurement errors associated with continuum placement for determining the line flux or errors in the distance measurement of the star or of other fundamental wind parameters (e.g., the mass-loss rate).

REFERENCES

- Abbott D. C., Biegging J. H., Churchwell E. B., 1981, *ApJ*, 250, 645
 Asida S. M., Tuchman Y., 1995, *ApJ*, 455, 286
 Balick B., 1987, *AJ*, 94, 671
 Barlow M. J., Hummer D. G., 1982, in *IAU Symp. #99*, p. 387
 Barlow M. J., Roche P. F., Aitken D. K., 1988, *MNRAS*, 232, 821
 Beals C. S. 1929, *MNRAS*, 90, 202
 Bjorkman J. E., & Cassinelli J. P., 1993, *ApJ*, 409, 429
 Bjorkman J. E., Ignace R., Tripp T. M., Cassinelli J. P., 1994, *ApJ*, 435, 416
 Bouret J.-C., Lanz T., Hillier D. J., 2005, *A&A*, 438, 301
 Brown J. C., Richardson L. L., Antokhin I., Robert C., Moffat A. F. J., St-Louis N., 1995, *A&A* 295, 725
 Brown J. C., Cassinelli J. P., Li Q., Kholtygin A. F., Ignace R., 2004, *A&A*, 426, 323
 Burrows C., et al., 1995, *ApJ*, 452, 680
 Cassinelli J. P., Brown J. C., Maheswaran M., Miller N. A., Telfer D. C., 2002, *ApJ*, 577, 951
 Crowther P. A., Hillier D. J., Evans C. J., Fullerton A. W., De Marco O., Willis A. J., 2002, *ApJ*, 579, 774
 Crotts A. P. S., Kunkel W. E., McCarthy P. J., 1989, *ApJ*, 347, L61
 Davies B., Oudmaijer R. D., Vink J. S., 2005, *A&A*, 439, 1107
 Dessart L., Crowther P. A., Hillier D., Willis A. J., Morris P. W., van der Hucht K. A., 2000, *MNRAS*, 315, 407
 Dessart L., Owocki S. P., 2002, *A&A*, 383, 1113
 Dessart L., Owocki S. P., 2003, *A&A*, 406, L1
 Dessart L., Owocki S. P., 2005, *A&A*, 432, 281
 Dorfi E. A., Höfner S., 1996, *A&A*, 313, 605
 Drew J. E., Barlow M. J., Unruh Y. C., Parker Q. A., Wesson R., Pierce M. J., Mashedier M. R. W. Phillipps S., 2004, *MNRAS*, 351, 206
 Feldmeier A., 1995, *A&A*, 299, 523
 Fullerton A. W., Massa D. L., Prinja R. K., 2006, *ApJ*, 637, 1025
 Hamann W. R., Koesterke L., 1998, *A&A*, 335, 1003
 Gräfener G., Koesterke L., Hamann W.-R., 2002, *A&A*, 387, 244
 Hamann W.-R., Gräfener G., 2003, *A&A*, 410, 993
 Hamann W.-R., Gräfener G., 2004, *A&A*, 427, 697
 Harries T. J., Hillier D. J., Howarth I. D., 1998, *MNRAS*, 296, 1072
 Hill G. M., Moffat A. F. J., St-Louis N., Bartzakos P., 2000, *MNRAS*, 318, 402
 Hill G. M., Moffat A. F. J., St-Louis N., 2002, *MNRAS*, 335, 1069
 Hillier D. I., 1991, *A&A*, 247, 455
 Howarth I. D., Prinja R. K., 1989, *ApJS*, 69, 527
 Ignace R., Cassinelli J. P., Quigley M., Babler B., 2001, *ApJ*, 558, 771
 Kingsburgh R. L., Barlow M. J., Storey P. J., 1995, *A&A*, 295, 75
 Kraus M., Miroshnichenko A. S., eds, 2006, *Stars with the B[e] Phenomenon*, ASP Conf. Ser.
 Lamers H. J. G. L. M., Cassinelli J. P. 1999, *Introduction to Stellar Winds*, New York, Cambridge University Press
 Lamers H. J. G. L. M., Cerruti-Sola M., Perinotto M., 1987, *ApJ*, 314, 726
 Lamers H. J. G. L. M., Najarro F., Kudritzki R. P., Morris P. W., Voors R. H. M., van Gent J. I., et al., 1996, *A&A*, 315, L229
 Lamers H. J. G. L. M., Pauldrach A. W. A., 1991, *A&A*, 244, L5
 Lepine S., Moffat A. F. J., Henriksen R. N., 1996, *ApJ*, 466, 392
 Lührs S., 1997, *PASP*, 109, 504
 Massa D., et al., 1995, *Apj*, 452, L53
 Meynet G., Maeder A., 2003, *A&A*, 404, 975
 Mihalas, D. 1978, *Stellar Atmospheres* (San Francisco: Freeman)
 Morris P. W., van der Hucht K. A., Crowther P. A., Hillier D. J., Dessart L., Williams P. M., Willis A. J., 2000, *A&A*, 353, 624
 Morris P. W., Crowther P. A., Houck J. R., 2004, *ApJS*, 154, 413
 Nota A., Livio M., Clampin M., Schulte-Ladbeck R., 1995, *ApJ*, 448, 788
 Nugis T., Crowther P. A., Willis A. J., 1998, *A&A*, 333, 956

- Osterbrock D. E., 1989, *Astrophysics of Gaseous Nebulae and Active Galactic Nuclei*, University Science Books
- Owocki S. P., Cranmer S. R., Gayley K. G. 1996, *ApJ*, 472, L115
- Pauldrach A. W. A., Puls J., 1990, *A&A*, 237, 409
- Petrenz P., Puls J., 2000, *A&A*, 358, 956
- Porter J. M., Rivinius Th., 2003, *PASP*, 115, 1153
- Poe C. H., Friend D. B., Cassinelli J. P., 1989, *ApJ*, 337, 888
- Pradhan A. K., Peng, J., 1995, in R.E. Williams and M. Livio, eds, *Analysis of Emission Lines*, Cambridge University Press, p. 8
- Runacres M. C., Owocki S. P., 2002, *A&A*, 381, 1015
- Runacres M. C., Owocki S. P., 2005, *A&A*, 429, 323
- Sakurai T., 1985, *A&A*, 152, 121
- Schulte-Ladbeck R. F., Nordsieck K. H., Taylor M., Bjorkman K. S., Magalhaes A. M., Wolff M. J., 1992, *ApJ*, 387, 347
- Schmutz W., Hamann W.-R., Wessolowski U., 1989, *A&A*, 210, 236
- Sean M., Balick B., 2004, *ApJ*, 615, 921
- Smith J.-D. T., Houck J. R., 2001, *AJ*, 121, 2115
- Smith J.-D. T., Houck J. R., 2005, *ApJ*, 622, 1044
- Soker N., 2000, *MNRAS*, 312, 217
- Stevens I R., Howarth, I. D., 1999, *MNRAS*, 302, 549
- Sugerman B. E. K., Crotts A. P. S., Kunkel W. E., Heathcote S. R., Lawrence S. S., 2005, *ApJS*, 159, 60
- Townsend R. H. D., Owocki S. P., 2005, *MNRAS*, 3457, 251
- ud-Doula A., Owocki S. P., 2002, *ApJ*, 576, 413 1998, *A&A*, 333, 251
- Underhill A. B., Gilroy K. K., Hill G. M., Dinshaw N., 1990, *ApJ*, 351, 666
- van der Hucht K. A., Morris P. W., Williams P. M., Setia Gunawan D. Y. A., Beintema D. A., Boxhoorn D. R., et al., 1996, *A&A*, 315, L193
- Verner K. T., Ferland G. J., 1996, *ApJS*, 103, 467
- Verner K. T., Ferland G. J., Korista K. T., Yakovlev D. G., 1996, *ApJ*, 465, 487
- Vreux J. M., Gosset E., Bohannan B., Conti P., 1992, *A&A*, 256, 148
- Washimi H., Shibata S., 1993, *MNRAS*, 262, 936
- Willis A. J., Dessart L., Crowther P. A., Morris P. W., Maeder, A., Conti P. S., van der Hucht K. A., 1997, *MNRAS*, 290, 371